The Exonuclease TREX1 Constitutes an Innate Immune Checkpoint Limiting cGAS/STING-Mediated Antitumor Immunity

Junghyun Lim, Ryan Rodriguez, Katherine Williams, John Silva, Alan G. Gutierrez, Paul Tyler, Faezzah Baharom, Tao Sun, Eva Lin, Scott Martin, Brandon D. Kayser, Robert J. Johnston, Ira Mellman, Lélia Delamarre, Nathaniel R. West, Sören Müller, Yan Qu, and Klaus Heger

ABSTRACT

The DNA exonuclease three-prime repair exonuclease 1 (TREX1) is critical for preventing autoimmunity in mice and humans by degrading endogenous cytosolic DNA, which otherwise triggers activation of the innate cGAS/STING pathway leading to the production of type I IFNs. As tumor cells are prone to aberrant cytosolic DNA accumulation, we hypothesized that they are critically dependent on TREX1 activity to limit their immunogenicity. Here, we show that in tumor cells, TREX1 restricts spontaneous activation of the cGAS/STING pathway, and the subsequent induction of a type I IFN response. As a result, TREX1 deficiency compromised *in vivo* tumor growth in mice. This delay in tumor growth depended on a functional immune system, systemic type I IFN signaling, and tumor-intrinsic cGAS expression. Mechanistically, we show that tumor TREX1 loss drove activation of $CD8^+$ T cells and NK cells, prevented $CD8^+$ T-cell exhaustion, and remodeled an immunosuppressive myeloid compartment. Consequently, TREX1 deficiency combined with T-cell–directed immune checkpoint blockade. Collectively, we conclude that TREX1 is essential to limit tumor immunogenicity, and that targeting this innate immune checkpoint remodels the tumor microenvironment and enhances antitumor immunity by itself and in combination with T-cell–targeted therapies.

See related article by Toufektchan et al., p. 673

Introduction

Immunotherapies targeting the T-cell checkpoints PD-1/PD-L1 and CTLA4 have provided substantial benefit to patients with cancer across multiple indications leading to durable long-lasting responses; however, this benefit is often limited to only a fraction of patients (1). This suggests that additional therapeutics affecting complementary nodes of an antitumor immune response and their combination with T-cell immune checkpoint inhibitors may be required to extend clinical benefit to a wider patient population (1, 2). For example, type I IFNs have been extensively explored as potential therapeutic agents (3–5). Type I IFNs are potent cytokines and clinically validated modulators of antiviral and anticancer immunity that function by enhancing antigen presentation, inducing dendritic cell (DC) maturation, increasing immune cell recruitment, and fostering the cytotoxic capacity of T and NK cells (3, 5). However, systemic agonism of the type I IFN pathway is associated with various toxicities limiting their clinical use (4). Thus, improving their therapeutic index remains a major elusive objective for the field. Current strategies include localized administration or targeted delivery of agonists to elicit a type I IFN response (3, 5). An alternative strategy could be the inhibition of negative regulators of type I IFN-inducing signaling pathways.

Three-prime repair exonuclease 1 (TREX1) is a non-processive 3′-5′ exonuclease degrading both single- and double-stranded DNA (6). It contains an N-terminal catalytic domain harboring its nuclease activity and a C-terminal transmembrane domain anchoring TREX1 to the ER and perinuclear envelope (6, 7). TREX1 plays a critical role in limiting the accumulation of cytosolic DNA species and thereby the activation of the innate double-stranded DNA sensor cGAS (6–9, 16). Subsequent production of the secondary messenger cGAMP by cGAS stimulates the ER-resident transmembrane protein STING. STING then translocates to the Golgi apparatus, where it recruits TBK1 leading to the phosphorylation and activation of IRF3 transcription factors and the successive induction of type I IFN expression (10). Indeed, TREX1-deficient mice develop autoimmune pathology associated with elevated type I IFN signaling and myocarditis, which is dependent on cGAS, STING, IRF3, and IFNAR1 (8, 11–14). In humans, various rare missense, nonsense, and frameshift mutations within the *TREX1* gene are linked to type I interferonopathies including Aicardi–Goutières syndrome (AGS), familial chilblains lupus (FCL), and systemic lupus erythematosus (SLE; refs. 15–17). Given that cancer cells are particularly prone to cytosolic DNA accumulation from various origins (18) and that TREX1 has been shown to restrict cGAS activation by degrading cytosolic DNA (6–9), we speculated that TREX1 would function as an innate immune checkpoint to limit the immunogenicity of tumor cells by restricting type I IFN production.

In this study, we showed that across multiple murine tumor cell lines genetic deficiency of TREX1 leads to STING activation and to a type I IFN response, and this was contingent on a functional cGAS/STING pathway but independent of additional DNA-damaging insults (19). TREX1 loss delayed tumor growth *in vivo* in mice. Genetic and pharmacologic approaches demonstrated that the attenuated growth of TREX1-deficient tumors was not cell intrinsic but dependent on a functional immune system, type I IFN signaling, and tumor-intrinsic

Genentech Inc., South San Francisco, California.

J. Lim and R. Rodriguez contributed equally to this article.

Y. Qu and K. Heger contributed equally as the co-senior author to this article.

Corresponding Author: Klaus Heger, Cancer Immunology, Genentech, Inc., 1 DNA Way, South San Francisco, CA 94080. E-mail: hegerk@gene.com

Cancer Immunol Res 2024;12:663–72

doi: 10.1158/2326-6066.CIR-23-1078

expression of the double-stranded DNA sensor cGAS. Detailed single-cell RNA sequencing (scRNA-seq) analysis revealed that mechanistically, tumor-specific TREX1 loss enhanced the cytotoxic capacity of $CD8^+$ T and NK cells and limited the exhaustion of $CD8^+$ T cells. In addition, TREX1 deficiency caused a remodeling of the immunosuppressive myeloid compartment within the tumor microenvironment (TME). Moreover, tumor-specific loss of TREX1 enhanced the potency of immune checkpoint blockade therapy. Collectively, our data implicate TREX1 as an innate immune checkpoint limiting tumor immunogenicity and suggest that inhibiting TREX1 may be an effective strategy for tumor immunotherapy.

Materials and Methods

Cell culture

CT26, EMT6, EO771, B16F10, and MC38 cell lines were obtained from the cell repository at Genentech. The CT26 (received in 2010), EMT6 (received in 2009), and B16F10 (received in 2005), cell lines were originally purchased from ATCC. The EO771 cell line was purchased from CH3 Biosystems (received in 2017). The MC38 cell line was obtained in 2012 from Dr. Ferry Ossendorp at the University of Leiden. Cell growth rates and morphology were monitored for any batch-to-batch changes. All stocks were tested for mycoplasma prior to and after cells were cryopreserved. Two methods of mycoplasma detection were used to avoid false positive/negative results: Lonza Mycoalert and Stratagene Mycosensor. In addition, CT26 and EO771 were authenticated by short tandem repeat (STR) profiling using the Promega PowerPlex 16 System. The MC38 cell line was cultured in DMEM (Corning, 50–013-PC) supplemented with 10% FBS (Gibco, 16140071), 2 mmol/L L-glutamine (Gibco, 35050061), and Pen/Strep (Gibco, 15140122). All other cell lines were cultured in RPMI1640 (Gibco, 31800022) supplemented with 10% FBS (Gibco, 16140071), 2 mmol/L L-glutamine (Gibco, 35050061), and Pen/Strep (Gibco, 15140122). Cells used in this study were not passaged more than six to seven times after thawing.

Cells knockout (KO) for TREX and/or cGAS were generated via CRISPR/Cas9-mediated deletion. Briefly, 2×10^5 tumor cells were electroporated (4D-Nucleofector; Lonza) with recombinant Cas9 (IDT) complexed with gene-specific sgRNAs (IDT). Two sgRNAs per gene were combined and nontargeting sgRNAs were used as a negative control. The following gene-specific seed sequences were used: *TREX1*, TTTCCTCGAACCATTCCCTG, AGGGTCTGCATGTGACCATG; NTC, CGTTAATCGCGTATAATACG, CATATTGCGCGTATAGTCGC; *CGAS*, ACGCAAAGATATCTCGGAGG, TGTTTAAACTGGAAGTCCCC.

A second independent TREX1 KO CT26 line (TREX1 KO CT26 #2) was purchased from Synthego. The sgRNA AGUGCCCAGACCGCCCCGUG targeting *TREX1* was used to generate a pool of cells with 96% TREX1 KO efficiency.

To generate TREX1 WT or TREX1 D18N expressing cells, pBCMV_Puro piggyBac backbone plasmids (Genentech) were engineered to carry N-terminal 3x FLAG-murine TREX1 WT or D18N genes. Empty plasmid (control), TREX1 WT or TREX1 D18N encoding plasmids were transfected together with a piggyBac transposase encoding plasmid (Genentech) by using Lipofectamine 3000 (Invitrogen). Transfected cells were selected using 10 μg/mL puromycin (Gibco, A1113803).

To generate STING-expressing MC38 cells, a plasmid was engineered to carry murine STING. In brief, a murine STING gene followed by a loxP-flanked IRES GFP 2A ERT2-Cre-ERT2 cassette was cloned downstream of an EF1a core promotor (to drive medium level expression mimicking endogenous levels) in a piggyBac backbone vector (Genentech). The STING encoding plasmid and a piggyBac transposase encoding plasmid were transfected using Lipofectamine 3000 (Invitrogen) and GFP-high expressing viable cells were sorted.

Cell line growth assay via incucyte

A total of 5×10^3 cells per well were plated in flat-bottom 96-well plates and analyzed in an Essen Incucyte Zoom (Essen Biosciences). Images were acquired with a 10× objective every 3 hours for a total of 72 to 96 hours. Cell growth was calculated by phase object confluence as % of total.

Western blotting

Cell pellets were lysed in RIPA buffer supplemented with protease and phosphatase inhibitors (Roche). Supernatants were obtained after centrifugation at 13,000 rpm for 15 minutes and protein concentration was measured using BCA assay (Thermo Fisher Scientific). Equal amounts of protein per sample were denatured in reducing sample buffer (Invitrogen). Proteins were separated on 4% to 12% gradient Bis-Tris gels (Novex) and subsequently transferred onto PVDF membranes (Bio-Rad). Membranes were incubated with antibodies against TREX1 (BD Biosciences, 611986, RRID:AB_399407, 1:4000), cGAS (Cell Signaling Technology, 31659, RRID:AB_2799008, 1:1000), p-STING (Ser365, Cell Signaling Technology, 72971, RRID:AB_2799831, 1:1,000), STING (Cell Signaling Technology, 13647, RRID:AB_2732796, 1:1,000), STAT1 (Cell Signaling Technology, 14994, RRID:AB_2737027, 1:4,000), β-actin (Cell Signaling Technology, 3700, RRID:AB_2242334 1:20,000), and ZBP1 (Novus, NBP2–80056, 1:4,000) in TBST with 5% nonfat dry milk (Bio-Rad). Binding was detected using the following secondary antibodies: rabbit IgG-HRP (Cell Signaling Technology, 7074, RRID:AB_2099233 1:4,000), mouse IgG-HRP (Cell Signaling Technology, 7076, RRID:AB_330924 1:4,000). Immunoblots were analyzed using enhanced chemiluminescence (Western lightning-plus ECL, Perkin Elmer).

ELISAs and luminex

A total of 1×10^5 cells per well were plated in flat-bottom 96-well plates for 48 hours and supernatants were collected. Mouse serum from whole blood was collected at the end of the *in vivo* study into vacutainer collection tubes (BD Biosciences). Snap frozen tumors were homogenized with nuclease-free hard tissue homogenizing mix 2.8 mm ceramic beads (OMNI International) by using a Bead Mill Homogenizer (OMNI International) in RIPA buffer supplemented with protease and phosphatase inhibitors (Roche). Tissue homogenates were centrifuged at 13,000 rpm for 15 minutes at 4°C and protein concentration was measured using BCA assay (Thermo Fisher Scientific). Equal amount of protein per sample was further diluted at least 10-fold in Millipore assay buffer. Aforementioned samples were analyzed for levels of cytokines CCL5, CXCL10, and IFNγ by using commercially available ELISA assays (R&D systems, DY478 and DY466) or Millipore Luminex multiplex assay (Hamilton Star platforms with Luminex FlexMap 3Ds).

Mice

Female BALB/c (RRID:IMSR_CRL:028) and NOD.Cg-*Prkdc*^{scid} *Il2rg*^{tm1Wjl}/SzJ (NSG, RRID:IMSR_JAX:005557) mice were purchased from Charles River Laboratories and Jackson Laboratory, respectively. All mice were housed at Genentech in individually ventilated cages within animal rooms maintained on a 14:10-hour, light:dark cycle. Animal rooms were temperature and humidity-controlled, between 68 and 79°F and 30% and 70%, respectively, with 10 to 15 room air

exchanges per hour. Mice were acclimated to study conditions for at least 3 days before tumor cell implantation. Genentech is AAALAC accredited, and all animal studies were reviewed and approved by Genentech's Institutional Animal Care and Use Committee (IACUC). All animals were maintained in accordance with the *Guide for the Care and Use of Laboratory Animals*.

In vivo tumor studies

A total of 1×10^5 cells resuspended in 100 μL of HBSS and Matrigel (BD Biosciences) mixture were inoculated into the subcutaneous space on the right flank of female BALB/c or NSG mice at 8 to 10 weeks of age. Tumors were measured with digital calipers that directly transmit and record measurement data. Tumors were measured two to three times per week. The following formula was used to calculate tumor volume, $V = 0.5 \times L \times W \times W$ (L is the length, W is the width). When tumors exceeded 125 mm^3, animals with similar sized tumors were selected and randomized into groups to minimize variance. Mice were closely monitored and euthanized if tumors ulcerated or volumes exceeded 2,000 mm^3. No mice showed body weight loss or adverse clinical signs during the studies.

For the anti-PD-1 efficacy study, mice were treated with isotype control antibodies (mouse IgG2a anti-gp120 LALAPG; Genentech) or anti-PD-1 (mouse IgG2a anti-PD-1; Genentech, clone GNE 9899). 10 mg/kg of antibody was administered intravenously for the first dose on day 0 (1 day after group out) and 5 mg/kg intraperitoneally three times per week for eight doses starting on day 2. Anti-PD-1 and isotype control antibodies were produced in-house at Genentech and were confirmed to be free of endotoxin contamination.

For the IFNAR1-blocking study, mice were treated with anti-IFNAR1 (mouse IgG1, clone MAR1–5A3, RRID:AB_2830518; Leinco Technologies) or isotype control (mouse IgG1; Genentech) antibodies. 500 μg of antibody was administered intraperitoneally starting 1 day before tumor inoculation for 3 consecutive days. Subsequently, for the remainder of the study, 250 μg of antibody was administered intraperitoneally three times weekly.

Tumor growth curves

Tumor growth curves were generated using a package of customized functions in R (R Foundation for Statistical Computing). Tumor volumes were subjected to natural log transformations before analysis, because tumors generally exhibit exponential growth. All raw tumor volume measurements from 0 to 8 mm^3 were judged to reflect complete tumor absence and were converted to 8 mm^3. A generalized additive mixed model was then applied to describe the changes in transformed tumor volumes over time using regression splines with automatically generated spline bases. This approach addresses both repeated measurements from the same study subjects and moderate dropouts before the end of the study.

RNA preparation for RT-qPCR and bulk RNA sequencing

Snap frozen mouse tumors were homogenized with nuclease-free hard tissue homogenizing mix 2.8 mm ceramic beads (OMNI International) by using a Bead Mill Homogenizer (OMNI International) in RLT buffer. Tissue homogenates were centrifuged at 13,000 rpm for 15 minutes at 4°C and the supernatants were processed for RNA isolation with an RNeasy Plus Mini Kit (Qiagen). Snap frozen cell pellets from cultured cell lines were directly lysed with RLT lysis buffer from the Rneasy Plus Mini Kit (Qiagen). Five hundred nanograms of RNA was used to generate cDNA with iScript cDNA Synthesis Kit (Bio-Rad). Diluted cDNA was mixed with gene-specific TaqMan probes and TaqMan Universal PCR master mix, and subjected to qPCR in a QuantStudio 5 Real-Time PCR System (Applied Biosystems). The following primer-probe sets were used: *Isg15*, Mm01705338_m1; *Ifit1*, Mm00515153_m1; *Mx1*, Mm00487796_m1; *Stat1*, Mm01257286_m1; *Hmbs*, Mm01143545_m1. Gene expression was calculated by the $2^{-\Delta Ct}$ method of individual transcript levels normalized to the *Hmbs* endogenous control.

Preparation of single-cell suspensions and staining for flow cytometry and sorting

Tumors were collected 10 days after tumor inoculation for scRNA-seq or 7 days after group out for flow cytometric analysis of immune cells. Group out was conducted when the implanted tumor volume exceeded 125 mm^3, animals with similar sized tumors within the range of 140 to 220 mm^3 were selected and randomized into groups to minimize variance. Tumors were weighed and homogenized using a Tumor Dissociation Kit (Miltenyi, 130–096–730) with a GentleMACS (Miltenyi, program TDK1). Cell suspensions were incubated in Fc receptor block (BD Biosciences, 2.4G2, #553142, RRID:AB_394657) and fixable viability dye (Invitrogen, 65–0865–14) in PBS. Cells were labeled with antibodies specific for surface antigens for 20 to 30 minutes at 4°C. For transcription factor staining, cells were fixed with FoxP3 Fixation Buffer (005523, eBioscience) for 30 minutes in the dark at room temperature. For cytoplasmic protein labeling, cells were fixed with Fixation buffer (554714; BD Biosciences) for 20 minutes at 4°C. Then, cells were stained with intracellular antibodies for 30 minute at 4°C. The following antibodies were used: BST2 (clone 927; BioLegend, RRID:AB_2562477), CD4 (clone RM4–5; BD Biosciences, RRID:AB_2870166), CD8 (clone KT15; MBL, RRID:AB_10597265), CD11b (clone M1/70; BD Biosciences, RRID:AB_2874105), CD11c (clone HL3; BD Biosciences, RRID:AB_2738580), CD19 (clone 6D5; BioLegend, RRID:AB_11218994), CD44 (clone IM7; BD Biosciences, RRID:AB_2870671), CD45 (clone 30-F11; BD Biosciences, RRID:AB_2870247), CD49b (clone DX5; BD Biosciences, RRID:AB_11153857), CD90.2 (clone 30-H12; BioLegend, RRID:AB_493725), F4/80 (clone BM8; BioLegend, RRID:AB_2564588), GZMB (clone GB12; Invitrogen, RRID:AB_10373420), LY6C (clone HK1.4; BioLegend, RRID:AB_2562351), LY6G (clone 1A8; BioLegend, RRID:AB_2566317), MHC-ll (clone M5/114.15.2; BD Biosciences, RRID:AB_2738192), and SCA-1 (clone D7; BD Biosciences, RRID:AB_2871229). Data were acquired on a symphony flow cytometer (BD Biosciences) or Cytek Aurora (Cytek Bioscience) and analyzed using FlowJo software (Version 10.9.0; FlowJo LLC, RRID:SCR_008520).

For scRNA-seq, cells were incubated with Fc receptor block and labeled with TotalSeq-C hashtag antibodies (clone M1/42;30-F11; BioLegend, hashtag 1–12) together with the following surface marker–specific antibodies: CD45 (clone 30-F11; BD Biosciences, RRID:AB_2870247), CD90.2 (clone 30-H12; BioLegend, RRID:AB_493725), CD31 (clone MEC13.3; BioLegend, RRID:AB_2572181), and PDGFRa (APA5; BioLegend, RRID:AB_2043969). Subsequently, cells were labeled with calcein blue (Invitrogen) and 7-AAD (BioLegend). Samples were sorted into T cells ($CD45^+CD90.2^+$), non-T immune cells ($CD45^+CD90.2^-$) and tumor cells ($CD45^-PDGFRa^-CD31^-$) with a FACSAria instrument (BD Biosciences). The same number of T cells and non-T immune cells from each animal per each population were pooled and duplicated for loading into a chromium single cell sorting system (10× Genomics).

Library preparation for scRNA-seq

Using the 10× Genomics Chromium Single Cell 5′ V2 Reagent Kit and Chromium Chip K Single Cell Kit, four samples of sorted single-cell suspensions were loaded onto the Chromium Controller. Each sample was loaded into two channels on the chip, targeting for 30,000

cell recovery per channel, effectively recovering 60,000 cells per sample. Cells from all samples were over 90% viable, with concentrations ranging from 1,430 to 1,770 cells/mL. GEMs were generated and cells were lysed, mRNA were barcoded and underwent reverse transcription to produce full-length cDNA. cDNA was amplified with 13 PCR cycles. Two types of libraries were generated (Gene Expression and Cell Surface Protein) according to manufacturer instructions.

Bulk RNA-seq of mouse tumor samples

Total RNA was quantified with the Qubit RNA HS Assay Kit (Thermo Fisher Scientific) and quality was assessed using RNA ScreenTape on a TapeStation 4200 (Agilent Technologies). For sequencing library generation, the TruseqStranded mRNA Kit (Illumina) was used with an input of 100 to 1,000 ng of total RNA. Libraries were quantified with Qubit dsDNA HS Assay Kit (Thermo Fisher Scientific) and the average library size was determined using D1000 ScreenTape on TapeStation 4200 (Agilent Technologies). Libraries were pooled and sequenced on NovaSeq 6000 (Illumina) to generate 30 million single-end 50-base pair reads for each sample.

scRNA-seq analysis

scRNA-seq fastq files were processed through the count utility from CellRanger (10× Genomics) using a custom reference generated from GENCODE M15 gene annotations and GRCm38/mm10. Multiplexed samples and antibody-specific barcodes were parsed using a wrapper to the DemuxEM package (20). The resulting UMI counts were read into Seurat (21) and TCR information was added to the metadata.

Cells were filtered for singlets marked by DemuxEM. Cells identified as singlets by scDblFinder (22) run with the samples option set to samples were retained. Cells were filtered for more than 500 genes expressed and less than 5% of reads from mitochondrial genes.

After each of the described filtering steps, data were processed as follows: Data were log-normalized using the *NormalizeData* function from Seurat. The top 2,000 variable features were selected using *FindVariableFeatures*, and the data were scaled using *ScaleData* from Seurat. Principal components (PC) were determined using *RunPCA*, and nearest neighbors were calculated using *FindNeighbors* with 30 PCs. The data were clustered to a specified resolution using *FindClusters* with 30 PCs. Uniform manifold approximation and projection (UMAP) plots were generated with 30 PCs using *RunUMAP*.

In a first step, cells were given broad cell type labels at a clustering resolution of 0.2. Cells that were not labeled as T or NK cells based on expression of typical markers such as *Cd3d* and *Ncr1* were removed from the $Cd90^+$ sort. Cells were separated by cell type into new objects, and remaining contaminating cells were identified and removed from each object. T cells were split into $CD4^+$ and $CD8^+$ T cells as classified by scGate (23). Using a clustering resolution of 1 and excluding TCR-encoding genes (*Tra, Trb*) from variable genes, we calculated clusters from which a remaining cluster of $Cd74^+$ cells was removed to obtain the final $CD8^+$ T-cell object. NK cells were clustered to a resolution of 1, and three remaining minor clusters of macrophages and T cells as well as cells with scores >0.5 for three non-negative matrix factorization (NMF) programs representing neutrophils, macrophages, and B cells were excluded. No additional filtering was performed for myeloid cells.

For the single-cell heatmaps, cells were ordered by the NMF program with the highest score for that cell followed by tumor genotype. The heatmap was created with DoHeatmap from Seurat (21).

Consensus NMF

Consensus NMF (cNMF) was run with number of components from 3 to 22, 20 iterations, and 2,000 genes (24). The number of components were chosen based on stability. Scores were normalized per cell. The number of components chosen for $CD8^+$ T cells was 10, and for myeloid cells nine components were used. Differences in NMF program usage between groups were assessed Wilcoxon rank-sum test in R.

Bulk RNA-seq analysis

Bulk RNA-seq data were processed using the BioConductor package HTSeqGenie (version 4.4.2, (https://bioconductor.org/packages/release/bioc/html/HTSeqGenie.html) as follows: first, reads with low nucleotide qualities (70% of bases with quality <23) or matches to rRNA and adapter sequences were removed. The remaining reads were aligned to the human reference genome (GRCm38.p5) using GSNAP (25) version "2013–11–01," allowing maximum of two mismatches per 75 base sequence (parameters: -M 2 -n 10 -B 2 -i 1 -N 1 -w 200000 -E 1 –pairmax-rna = 200000′). Transcript annotation was based on the Gencode genes data base (GENCODE M15). To quantify gene expression levels, the number of reads mapping unambiguously to the exons of each gene was calculated. For the bulk RNA-seq from *in vivo* tumor cells, one sample was removed based on low number of reads.

Differential expression analysis

For scRNA-seq, average expression of raw counts was calculated per animal, and animals with fewer than 200 cells were removed. For both scRNA-seq and bulk RNA-seq differentially expressed genes were calculated using edgeR and called as significant if *P* value was less than 0.05 for scRNA-seq or 0.01 for bulk RNA-seq (26, 27). For bulk *in vivo* tumor samples, principal component analysis was calculated using *prcomp* from the stats package (R Core Team (2021). R: A language and environment for statistical computing. R Foundation for Statistical Computing (https://www.R-project.org/), which accounted for immune cell contamination. Principal component 1 was added as a covariate for differential expression analysis in edgeR.

GO analysis

GO analysis was performed using the enrichGO function from clusterProfiler (28) using all biological processes and FDR as the *P* value adjustment method.

Statistical analyses

All results are presented as the means of data with SEM or SD as described in figure legends. Pairwise statistical analyses were performed using an unpaired Student two-sided *t* test or unpaired *t* test with Welch correction. Correction for multiple-comparisons was performed using the Holm–Sidak method with $a = 0.05$. Studies with three groups were analyzed with one-way ANOVA followed by multiple comparison. Analysis of survival was performed using log-rank test. Analysis of tumor growth was performed using two-way ANOVA or two-way ANOVA with a mixed-effect model followed by Tukey multiple comparison testing. GraphPad Prism (RRID: SCR_002798) was used for data analysis and representation.

Data availability

The data generated in this study are available in the article and its supplementary files or upon reasonable request from the corresponding author. Bulk RNA-seq and scRNA-seq datasets generated in this study have been deposited in the ArrayExpress database under accession codes: E-MTAB-13823 (scRNA-seq), E-MTAB-13815 (bulk RNA-seq TREX1 KO cell lines), and E-MTAB-13816 (bulk RNA-seq sorted CT26 tumors *in vivo*).

Results

TREX1 loss causes cGAS/STING activation and induction of a type I IFN signature in murine tumor cell lines

To explore the consequences of TREX1 loss across a range of common murine tumor cell lines, we employed CRISPR/Cas9 gene editing to generate TREX1-deficient CT26, EO771, EMT6, B16F10, and MC38 cell lines (**Fig. 1A**). Western blotting confirmed high efficiency of TREX1 ablation in bulk nonclonal populations (**Fig. 1A**). In CT26, EO771, and EMT6 tumor cell lines, genetic TREX1 loss led to spontaneous activation of the cGAS/STING pathway and the induction of IFN-stimulated genes (ISG), as indicated by increased STING phosphorylation, ZBP1 expression, and secretion of the IFN-induced chemokines CCL5 and CXCL10 (**Fig. 1A** and **B**). Results in the CT26 cell line were validated with a second independently generated bulk nonclonal TREX1 KO population (Supplementary Figs. S1B and S1C). B16F10 cells showed a slightly muted but still detectable response upon TREX1 loss (**Fig. 1A** and **B**). Additional bulk RNA-seq of CT26, EO771, EMT6, and B16F10 cells cultured *in vitro* confirmed a selective increase in expression of ISGs as indicated by gene ontology pathways related to "response to virus" and "cellular response to IFNβ" (Supplementary Fig. S1A). In contrast, in the MC38 tumor cell line, TREX1 deficiency did not cause spontaneous ISG induction (**Fig. 1A** and **B**). This was due to the absence of endogenous STING expression, as reintroduction of STING increased IFN-induced chemokine production upon genetic TREX1 loss (Supplementary Figs. S1D and S1E). TREX1 deficiency did not affect the survival or proliferation of CT26, EO771, EMT6, B16F10, and MC38 cell lines in culture *in vitro* (Supplementary Fig. S1F). Collectively, these data indicate that TREX1 deficiency leads to spontaneous type I IFN signaling in multiple murine tumor cell lines, and that this depends on a functional cGAS/STING pathway.

Tumor-intrinsic TREX1 loss impairs CT26 tumor growth in immunocompetent mice

To investigate the physiologic significance of TREX1 loss on *in vivo* tumor growth, we implanted control and TREX1-deficient CT26 tumor cells into immunocompetent BALB/c and immunodeficient NSG hosts, the latter lack innate and adaptive lymphocytes including T, B, and NK cells. Although TREX1 deficiency in CT26 cells had minimal effects on tumor growth in immunodeficient NSG hosts, it caused impaired tumor growth in immunocompetent BALB/c animals (**Fig. 2A**; Supplementary Fig. S2A). Chemokine quantification in tumor lysates showed an increase in CCL5 and CXCL10 levels upon TREX1 deficiency in NSG animals, which was further exacerbated in BALB/c hosts, indicating that innate and/or adaptive lymphocytes amplify an initial response (Supplementary Fig. S2B). Bulk RNA-seq analysis and qRT-PCR measurement of ISG expression in CT26 cells sorted from BALB/c hosts confirmed an ISG signature in TREX1-deficient compared with control tumor cells (**Fig. 2B**; Supplementary Figs. S2C and S2D). Consistently, the *in vivo* growth delay was normalized upon pharmacologic inhibition of the type I IFN receptor 1 (IFNAR1; **Fig. 2C**; Supplementary Fig. S2E). Together these results demonstrate that enhanced type I IFN signaling due to tumor-intrinsic TREX1 loss causes a tumor growth delay in immunocompetent mice.

Cellular activation caused by TREX1 deficiency is cGAS dependent

To understand the contribution of TREX1's catalytic activity to limiting cGAS/STING pathway activation, we expressed FLAG-tagged WT or catalytic dead (D18N) TREX1 in control and TREX1-deficient CT26 cells (29). WT but not D18N TREX1 was able to rescue the higher STING phosphorylation in TREX1 KO CT26 tumor cells (Supplementary Fig. S3A). To further understand if the accumulation of aberrant DNA species drives the phenotype in TREX1-deficient

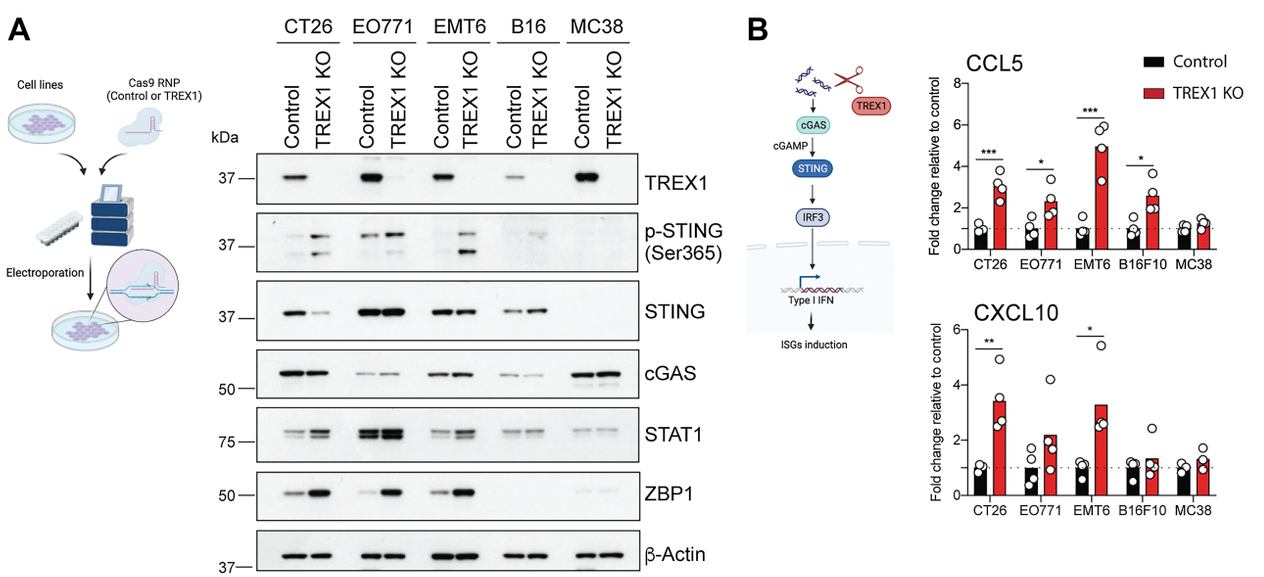

Figure 1.
TREX1 limits a cGAS/STING-induced ISG response in multiple common murine tumor cell lines. **A,** Schematic of Cas9/gRNA-mediated TREX1 deletion in tumor cell lines (left). Representative Western blots of TREX1, p-STING (Ser365), STING, cGAS, STAT1, ZBP1, and β-actin in control and TREX1 KO cell lines (right; $n = 4$). **B,** Schematic of the cGAS/STING pathway (left). CCL5 and CXCL10 protein levels in supernatants. Values normalized to the average of control samples. Circles represent independent experiments. Bars represent the mean ($n = 3$–4). Unpaired t test. *, $P < 0.05$; **, $P < 0.01$; and ***, $P < 0.001$.

tumors, we deleted the double-stranded DNA sensor cGAS (**Fig. 2D**). Loss of cGAS reduced the spontaneous STING phosphorylation and secretion of CCL5 and CXCL10 in TREX1-deficient cells (**Fig. 2D** and **E**). Loss of cGAS even in TREX-proficient control CT26 cells led to a reduction in the mild steady-state activation, which was mimicked by expression of WT TREX1 on top of endogenous TREX1 (**Fig. 2D** and **E**; Supplementary Fig. S3A). Collectively, these data suggest that low steady-state activation of the cGAS/STING pathway occurs in CT26 tumor cells, but is kept in check by TREX1 and exacerbated upon its loss. Implantation of control, TREX1 KO, cGAS KO, and TREX1 cGAS double KO (dKO) tumors in BALB/c mice demonstrated that the slow tumor growth of TREX1-deficient cells is cGAS dependent (**Fig. 2F**; Supplementary Fig. S3C). In contrast, these cell lines proliferated similarly *in vitro* (Supplementary Fig. S3B). Consistent with these findings, increased ISG expression in TREX1-deficient tumors *in vivo* was rescued by cGAS loss (**Fig. 2G**). Thus, TREX1 limits STING

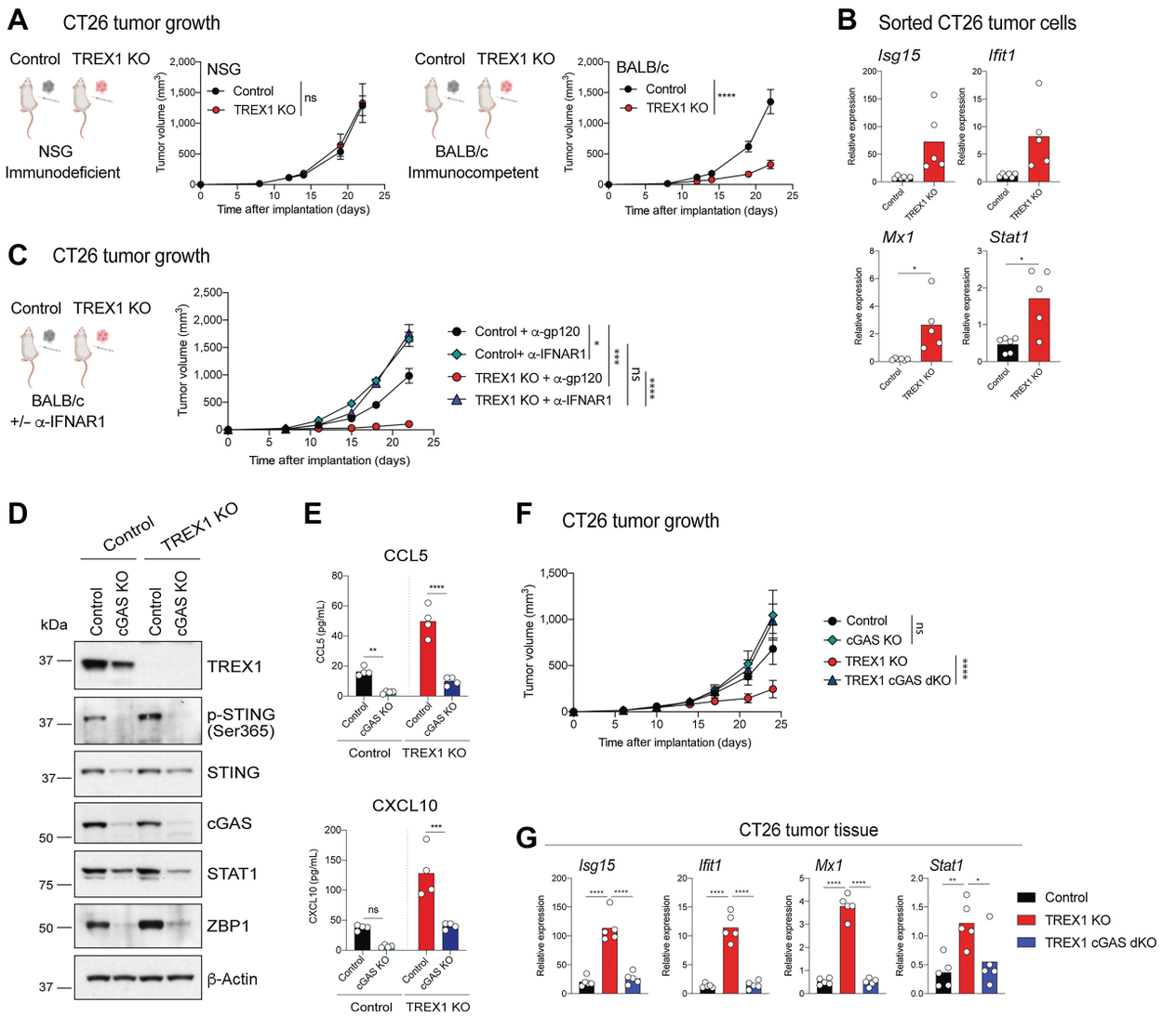

Figure 2.

Tumor-intrinsic TREX1 loss results in impaired CT26 tumor growth in immunocompetent mice in a type I IFNs and cGAS-dependent manner. **A,** Control and TREX1 KO CT26 tumor growth curves in immunodeficient NSG and immunocompetent BALB/c hosts. Lines represent the mean ± SEM. Two-way ANOVA (NSG, $n = 6$; BALB/c, $n = 10$ per group). **B,** RT-qPCR analysis of *Isg15*, *Ifit1*, *Mx1*, and *Stat1* mRNA expression levels in sorted ($CD45^-CD31^-PDGFRa^-$) CT26 tumor cells isolated from BALB/c hosts. Circles represent individual animals. Bars represent the mean. Unpaired *t* test with Welch correction (control, $n = 6$; TREX1 KO, $n = 5$). **C,** Control and TREX1 KO CT26 tumor growth curves in BALB/c hosts ± IFNAR1 blockage. Lines represent the mean ± SEM. Tumor volume at the last time point was compared by Two-way ANOVA using a mixed-effect model followed by Tukey multiple comparisons ($n = 10$ per group). **D,** Representative Western blots of TREX1, p-STING (Ser365), STING, cGAS, STAT1, ZBP1, and β-actin in CT26 cell lines of the indicated genotype ($n = 4$). **E,** CCL5 and CXCL10 protein levels in supernatants. Circles represent independent experiments. Bars represent the mean. Multiple *t* test ($n = 4$). **F,** Control, TREX1 KO, cGAS KO and TREX1 cGAS dKO CT26 tumor growth curves in BALB/c hosts. cGAS KO and TREX1 KO cGAS dKO groups were compared to control and TREX1 KO, respectively, by Two-way ANOVA using a mixed-effects model. Lines represent the mean ± SEM. (TREX1 KO $n = 10$; Control, cGAS KO, TREX1 cGAS dKO $n = 9$ per group). **G,** RT-qPCR analysis of *Isg15*, *Ifit1*, *Mx1*, and *Stat1* mRNA expression levels in CT26 tumor tissue. Circles represent individual animals. Bars represent the mean. One way ANOVA ($n = 5$). ns, $P > 0.05$; *, $P < 0.05$; **, $P < 0.01$; ***, $P < 0.001$; and ****, $P < 0.0001$.

activation via its catalytic activity. Hence, the phenotypes of TREX1 loss, including *in vivo* tumor growth, are rescued by concurrent loss of the double-stranded DNA sensor cGAS.

TREX1 loss remodels the tumor immune microenvironment

Given that TREX1-deficient tumor cells showed a growth delay in immunocompetent but not immunodeficient hosts (**Fig. 2A**), we characterized the consequences of CT26 tumor-intrinsic TREX1 loss on the host immune system by performing scRNA-seq on intratumoral immune cells sorted from control and TREX1 KO CT26 tumors (Supplementary Fig. S4A). After quality control, we performed dimensionality reduction using the UMAP algorithm on 86,134 single cells passing quality control with a mean of 2,150 detectable genes per cell. This yielded both myeloid and lymphoid populations with the expected immune cells being present in both control and TREX1-deficient CT26 tumors (Supplementary Fig. S4B). Mononuclear phagocytes [macrophages, monocytes, and type 2 conventional DCs (cDC2); MoMacs] and CD8$^+$ T cells from control and TREX1 KO CT26 tumors occupied distinct areas of the UMAP, suggesting that tumor TREX1 loss impacted these immune cell subsets (Supplementary Fig. S4C). Pseudo-bulk differential expression analysis across all immune cells showed increased ISG expression in cells sorted from TREX1 KO compared with control tumors (Supplementary Fig. S4C). Further flow cytometric analysis indicated that the ISG induction upon tumor-intrinsic TREX1 loss occurred across the majority of immune cell types in the TME (Supplementary Fig. S4D).

We next performed deeper analysis of MoMacs (**Fig. 3A**). Pseudo-bulk analysis suggested that CT26 tumor-intrinsic TREX1 loss had a strong cell extrinsic influence on these immune cells, with an increase in multiple ISGs including *Ly6c1*, *Ly6c2*, *Bst2*, *Ly6a*, *Irf7*, *Isg15*, and *Rsad2*, accompanied by a decrease in the complement proteins *C1qa*, *C1qb*, and *C1qc* (**Fig. 3B**). Flow cytometric analysis confirmed an increase in SCA-1 (encoded by *Ly6a*), LY6C, and BST2 expression on myeloid cells from TREX1-deficient compared with control tumors

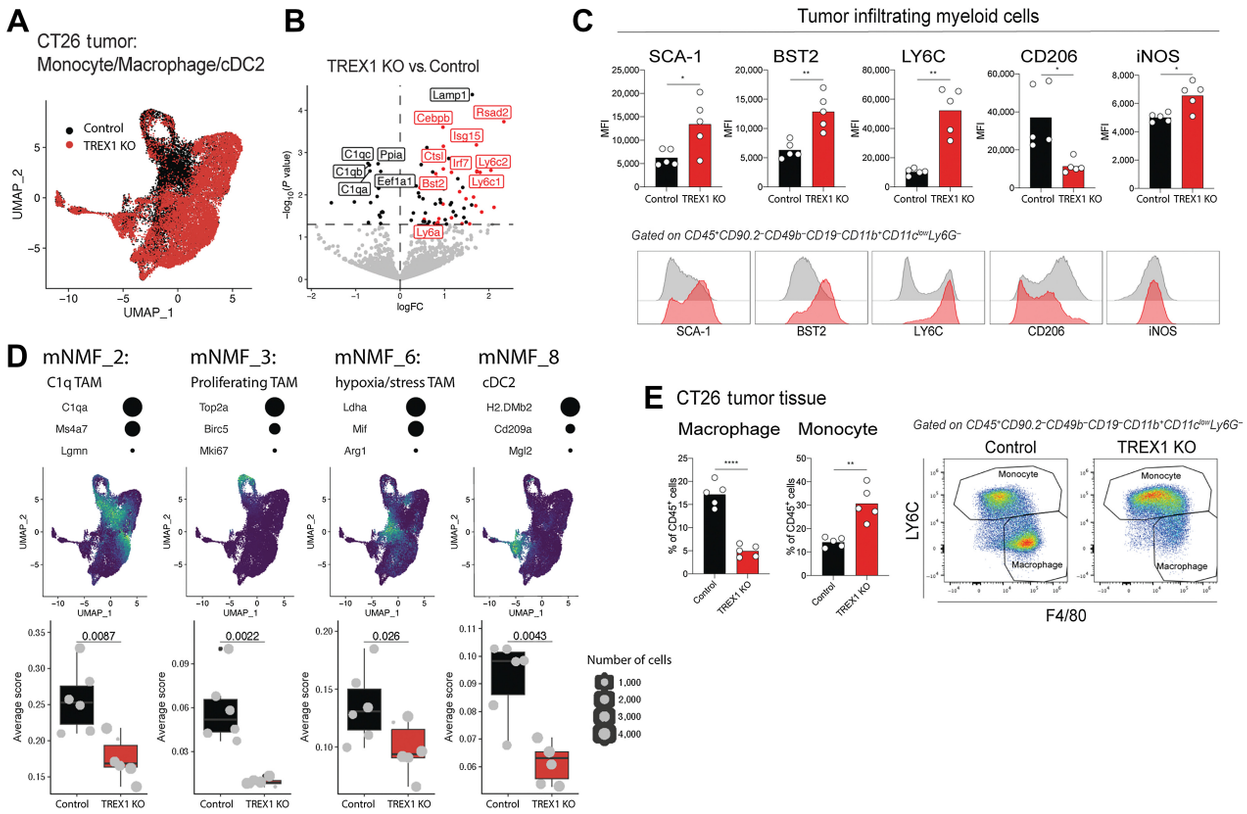

Figure 3.

TREX1 loss remodels an immunosuppressive myeloid TME. **A,** UMAP of monocytes, macrophages, and cDC2s in control and TREX1 KO CT26 tumors following scRNA-seq analysis. Cells are colored according to tumor genotype. **B,** Volcano plot showing genes differentially expressed comparing pseudobulk of tumor-infiltrating myeloid cells in control and TREX1 KO CT26 tumors. Horizontal dashed line represents a *P* value cutoff of 0.05. ISGs are highlighted in red. The five genes with the lowest *P* value in both directions are labeled in addition to *Irf7*, *Ly6c2*, *Ly6c1*, *Bst2*, and *Ly6a*. Only animals with more than 200 cells were included. **C,** Bar graphs and representative flow cytometry histograms of SCA-1, BST2, LY6C, CD206, and iNOS expression on myeloid cells in control and TREX1 KO CT26 tumors. Circles represent individual animals. Bars represent the mean. Unpaired *t* test with Welch correction ($n = 5$ per group). *, $P < 0.05$; **, $P < 0.01$. **D,** Four NMF programs from monocytes, macrophages, and cDC2s (mNMF) with significantly different scores comparing control and TREX1 KO CT26 tumors. Three representative genes for each program are listed with dots sized according to their relative contribution to the NMF program. UMAPs show scaled program scores for the given NMF program from low (blue) to high (yellow). Box plots display the NMF scores averaged by animal (grey points). Size of the points represents the number of cells for each animal. Points extended >1.5× interquartile range from the hinge are shown as outliers (marked by a black dot). Whiskers represent the minimum and maximum. The box represents the interquartile range, and the center line represents the median. Wilcox rank-sum test. **E,** Bar graphs and representative flow cytometry plots showing monocyte and macrophage proportions in CT26 tumors. Circles represent individual animals. Bars represent the mean ($n = 5$). Unpaired *t* test with Welch correction. **, $P < 0.01$; ****, $P < 0.0001$.

(**Fig. 3C**). NMF identified nine programs, to which we assigned function based on biologically relevant contributing genes (mNMF1–9, **Fig. 3D**; Supplementary Figs. S5A and S5B, Supplementary Table S1). Upon TREX1 loss, we observed a decrease in a C1q tumor-associated macrophage (TAM) program (mNMF_2: *C1qa*, *C1qb, C1qc, Ms4a7*, *Lgmn*), a TAM proliferation program (mNMF_3: *Top2a*, *Birc5*, *Mki67*), a cDC2 cell identity program (mNMF_8: *H2.DMb2*, *Cd209a*, *Mgl2*), and a hypoxia/stress TAM program (mNMF_6: *Arg1*, *Mif*, *Ldha*). Flow cytometric analysis demonstrated an overall reduction in macrophages in TREX1 KO compared with control tumors (**Fig. 3E**), which was rescued upon concurrent tumor-intrinsic cGAS loss (Supplementary Fig. S5C). Collectively, these data highlight that tumor-intrinsic TREX1 loss remodels the myeloid compartment in the TME, leading to a reduction in potentially immunosuppressive myeloid cell programs (C1q and hypoxia/stress TAM).

Similar to monocytes and macrophages, tumor-infiltrating CD8$^+$ T cells also showed a strong increase in ISGs including *Ly6c* and *Ly6a*, as well as an increase in the cytotoxic mediators *Gzma* and *Gzmb* (**Fig. 4A** and **B**). This is consistent with flow cytometric analysis demonstrating increased SCA-1 and GZMB expression by CD8$^+$ TILs (**Fig. 4C**). In addition, CD8$^+$ T cells isolated from TREX1-deficient tumors displayed higher *Ccl5* expression consistent with the tumor not being the sole source of CCL5 (**Fig. 4B**; Supplementary Fig. S2B). To further identify programs that explain the observed differences in CD8$^+$ T cells from control and TREX1 KO CT26 tumors, we

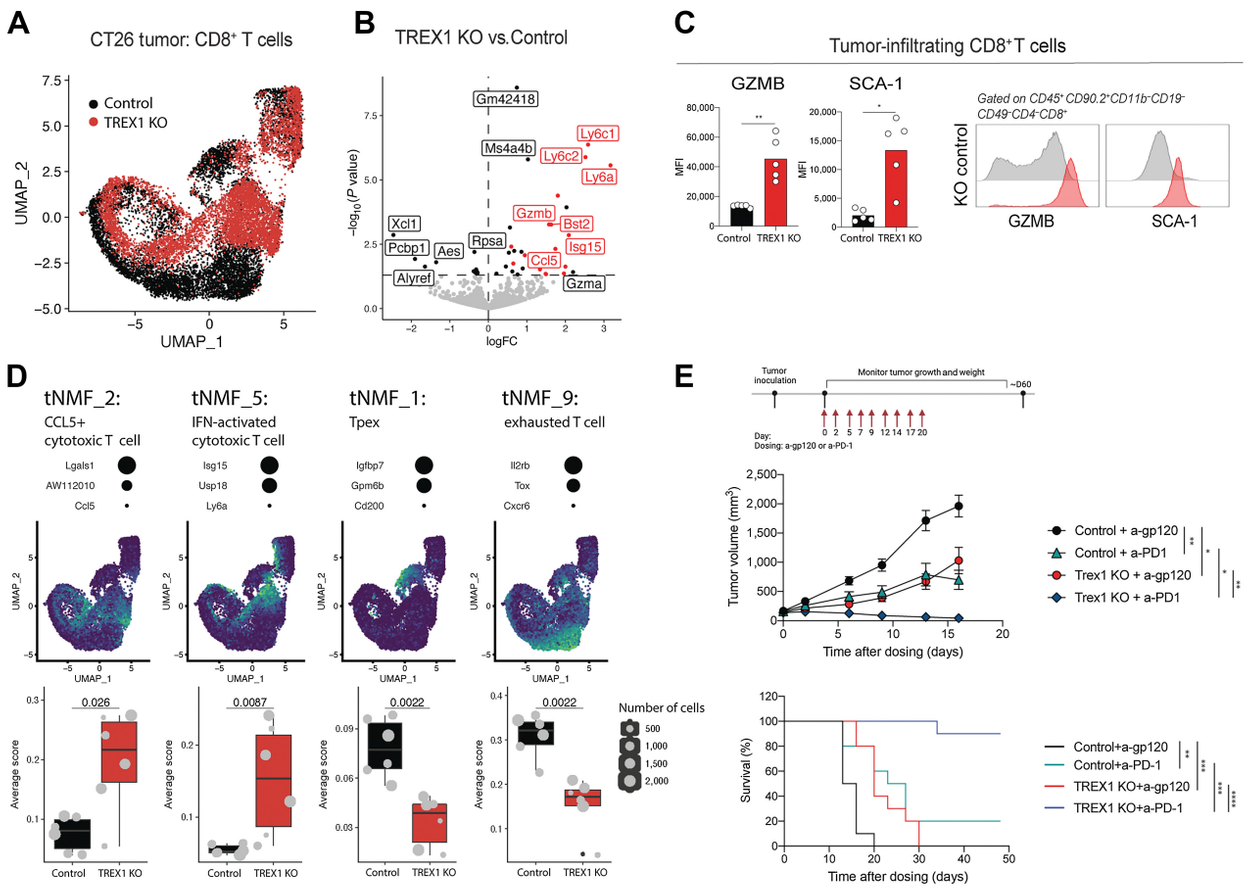

Figure 4.

TREX1 loss increases CD8$^+$ T-cell activation, limits their exhaustion, and enhances the potency of immune checkpoint blockade therapy. **A,** UMAP of CD8$^+$ T cells in control and TREX1 KO CT26 tumors following scRNA-seq analysis. Cells are colored according to tumor genotype. **B,** Volcano plot showing genes differentially expressed comparing pseudobulk of tumor-infiltrating CD8 T cells in control and TREX1 KO CT26 tumors. Horizontal dashed line represents a *P* value cutoff of 0.05. ISGs are highlighted in red. The five genes with the lowest *P* value in both directions are labeled in addition to *Gzmb*, *Bst2*, *Isg15*, *Ccl5*, and *Gzma*. Only animals with more than 200 cells were included for comparison. **C,** Bar graphs and representative flow cytometry histograms showing expression of GZMB, and SCA-1 on CD8$^+$ T cells in CT26 tumors. Circles represent individual animals. Bars represent the mean. Unpaired *t* test with Welch correction ($n = 5$ per group). *, $P < 0.05$; **, $P < 0.01$. **D,** Four NMF programs from CD8$^+$ T cells (tNMF) with significantly different scores in TREX1 KO and control CT26 tumors. Three representative genes for each program are listed with dots sized according to their relative contribution to the NMF program. UMAPs show scaled program scores for the given NMF program from low (blue) to high (yellow). Box plots display the NMF scores averaged by animal (grey points). Size of the points represents the number of cells for each animal. Points extended >1.5× interquartile range from the hinge are shown as outliers (marked by a black dot). Whiskers represent the minimum and maximum. The box represents the interquartile range, and the center line represents the median. Wilcox rank-sum test. **E,** Tumor growth (top) and survival curves (bottom) of control and TREX1 KO CT26 upon anti-PD1 or isotype antibody treatment. Tumor volume at the last time point was compared by ANOVA using a mixed-effect model followed by Tukey's multiple comparisons. Lines represent the mean ± SEM ($n = 10$ per group). Survival was assessed with log-rank test. Lines represent median survival. Tumor volumes larger than 2,000 mm^3 was regarded as end point ($n = 10$ per group). *, $P < 0.05$; **, $P < 0.01$; ***, $P < 0.001$; ****, $P < 0.0001$.

performed NMF. Within the 10 identified programs, five states were significantly altered (tNMF_1–10; **Fig. 4D**; Supplementary Figs. S6A and S6B, Supplementary Table S2): an IFN-activated cytotoxic T-cell program (tNMF_5: *Isg15*, *Usp18*, *Irf7*, and *Ly6a* among other ISGs) and a CCL5+ cytotoxic T-cell program (tNMF_2: *Ccl5*, *Lgals1*, *AW112010*) were induced in TREX1 KO versus control tumors, whereas programs consistent with precursor exhausted T cells (Tpex, tNMF_1: *Igfbp7*, *Gpm6b*, *CD200*), exhaustion (tNMF_9: *Il2rb*, *Tox*, *Cxcr6*), and proliferation (tNMF_6: *Ranbp1, Mcm3*) were reduced (**Fig 4D**; Supplementary Figs. S6A and S6B). Similar to $CD8^+$ T cells, tumor-infiltrating NK cells showed an increase in expression of ISGs (*Ifi27l2a*, *Ly6a*, *Ly6c2*, *Irf7*) and the cytotoxic mediator *Gzmb* (Supplementary Figs. S6C and S6D). This is consistent with our flow cytometric analysis showing increased SCA-1 and GZMB expression by NK cells (Supplementary Fig. S6F), which was dependent on tumor-intrinsic cGAS expression (Supplementary Fig. S6G). Moreover, concordant with the enhanced activation of $CD8^+$ T cells and NK cells in TREX1-deficient CT26 tumors, we detected an increase in type II IFN protein levels within the tumor (Supplementary Fig. S6E), likely contributing to the ISG response observed *in vivo* (**Fig. 2B** and **G**; Supplementary Figs. S2B–S2D). Overall, these data suggest that tumor-intrinsic TREX1 loss favors T-cell states associated with improved effector potential (IFN-activated and $CCL5^+$ cytotoxic T cells) while limiting their exhaustion (Tpex and exhausted T cells).

Tumor TREX1 loss combines with T-cell–directed immune checkpoint blockade

We next assessed the efficacy of tumor-specific TREX1 loss in combination with immune checkpoint blockade. CT26 tumor growth was only delayed by either single agent therapy with a PD-1 blocking antibody or genetic TREX1 deficiency. In contrast, combination of anti-PD-1 treatment and genetic TREX1 loss induced complete tumor regression and prolonged survival in a majority of animals (**Fig. 4E**; Supplementary Figs. S6H and S6I). Thus, genetic tumor-intrinsic TREX1 deletion can combine with T-cell–directed checkpoint inhibitors to promote tumor control and antitumor $CD8^+$ T-cell responses.

Discussion

Type I IFNs are known for their central role in driving antitumor immunity and have been approved for the treatment of various hematopoietic and solid malignances (3–5). However, systemic type I IFN agonists cause diverse toxicities, which, among other considerations, led to their replacement with more efficacious and safer immunotherapeutics (4). Clinical insights from the T-cell field indicate that systemic activation of pathways with agonists including IL-2 or IL-12 is often constrained by poor tolerability (4). In contrast, targeting negative regulators of T-cell activation including the checkpoints PD-1/PD-L1 and CTLA4 comes with a much better safety profile as these approaches are thought to predominantly amplify endogenous responses in contrast to broadly activating T cells (1, 2). Analogous to adaptive T-cell checkpoints, targeting negative regulators of type I IFN–inducing innate signaling pathways (innate immune checkpoints) may feature an improved safety profile relative to systemic agonism.

Here, we demonstrate that TREX1 in tumor cells functions as a key innate immune checkpoint restricting type I IFN and cGAS-dependent tumor immunogenicity. This is in line with the rescue of autoimmune pathology in germline TREX1-deficient mice through genetic loss of IFNAR1 or the double-stranded DNA sensor cGAS (8, 11, 14). The cGAS-activating cytosolic DNA species in TREX1-deficient murine tumor cells currently remains undefined and warrants further investigation. However, in contrast to previous reports (19), this DNA species appears to arise spontaneously in TREX1 KO malignant cells independent of additional DNA-damaging insults and hence might be due to the reactivation of endogenous retroelements, chromosomal instability leading to the generation of labile micronuclei, or products generated during uncontrolled proliferation as part of DNA repair or replication (8, 9, 18, 30, 31). Because of aberrant spontaneous cytosolic DNA accumulation (18), cancer cells may be more dependent on TREX1 than normal cells to limit their immunogenicity. Therefore, pharmacologic inhibition may predominantly elicit a tumor-specific response sparing healthy tissues. However, understanding the therapeutic index of systemic TREX1 inhibition will be important for clinical translation, as human genetic data link *TREX1* loss-of-function mutations to various type I interferonopathies, including AGS, FCL, and SLE (15–17), and TREX1-deficient mice develop autoimmunity and inflammatory myocarditis (8, 11–14).

Type I IFNs are thought to have antitumor effects through enhancing host immune responses by acting on both innate and adaptive immune cells (3, 5). Consistently, we show that improved tumor control due to TREX1 loss was dependent on a functional immune system, based on the loss of this phenotype in immunodeficient animals. Single-cell analysis demonstrated that TREX1 deficiency caused a substantial remodeling of the tumor myeloid compartment leading particularly to a reduction in various macrophage populations. Interestingly, hypoxia/stress TAMs, often also referred to as $SPP1^+$ TAMs, have recently attracted substantial interest as they are intimately associated with immunosuppression in the TME in addition to poor clinical outcome (32, 33). In addition, T cells are essential drivers of antitumor immunity and tumor-infiltrating T cells are a well-established correlate of favorable prognosis and responsiveness to immunotherapy (34). However, in response to repetitive antigen stimulation and harsh environmental conditions, most tumor-infiltrating T cells become functionally exhausted and lose the ability to constrain tumor growth (35). $CD8^+$ T-cell exhaustion is thought to occur via precursor cells known as Tpex and requires several key transcription factors including the homeobox protein TOX (35). Notably, we observed clear reductions of both Tpex and *Tox*-expressing exhausted T-cell programs in TREX1-deficient tumors, whereas $CD8^+$ T-cell states associated with a cytotoxic gene expression profile were increased. Therefore, a remodeling of the TME myeloid compartment that alleviates its immunosuppressive effects combined with enhanced $CD8^+$ T-cell effector function makes TREX1-deficient tumors likely more amenable to immune checkpoint blockade.

Collectively, these results implicate the exonuclease TREX1 as a key innate immune checkpoint and a potential target for tumor immunotherapy to enhance antitumor immunity by itself or in combination with T-cell–targeted therapies.

Authors' Disclosures

J. Lim reports other support from Genentech outside the submitted work. K. Williams reports other support from Genentech outside the submitted work. J. Silva reports other support from Genentech outside the submitted work. A.G. Gutierrez reports other support from Genentech outside the submitted work. P. Tyler reports other support from Genentech outside the submitted work. F. Baharom reports other support from Genentech outside the submitted work. T. Sun reports other support from Genentech outside the submitted work. E. Lin reports other support from Genentech outside the submitted work. S.E. Martin reports other support from Genentech outside the submitted work. B.D. Kayser reports other support from Genentech outside the submitted work. R.J. Johnston reports other support from Genentech outside the submitted work. I. Mellman reports other

support from Genentech during the conduct of the study; other support from Genentech outside the submitted work. L. Delamarre reports other support from Genentech outside the submitted work; and reports employment with Genentech. N. R. West reports other support from Genentech outside the submitted work. S. Müller reports ownership interest (including stock, patents) in Roche/Genentech. Y. Qu reports other support from Genentech outside the submitted work. K. Heger reports other support from Genentech, Inc. outside the submitted work. No disclosures were reported by the other authors.

Authors' Contributions

J. Lim: Conceptualization, investigation, writing–original draft. **R. Rodriguez:** Investigation, writing–review and editing. **K. Williams:** Formal analysis, writing–review and editing. **J. Silva:** Investigation, writing–review and editing. **A.G. Gutierrez:** Investigation, writing–review and editing. **P. Tyler:** Investigation, writing–review and editing. **F. Baharom:** Investigation, writing–review and editing. **T. Sun:** Investigation, writing–review and editing. **E. Lin:** Investigation, writing–review and editing. **S. Martin:** Conceptualization, writing–review and editing. **B.D. Kayser:** Conceptualization, formal analysis, writing–review and editing. **R.J. Johnston:** Conceptualization, writing–review and editing. **I. Mellman:** Conceptualization, writing–review and editing. **L. Delamarre:** Conceptualization, writing–review and editing. **N.R. West:** Conceptualization, writing–review and editing. **S. Müller:** Conceptualization, formal analysis, writing–review and editing. **Y. Qu:** Conceptualization, supervision, writing–review and editing. **K. Heger:** Conceptualization, supervision, investigation, writing–original draft.

Acknowledgments

We thank the Genentech flow core laboratory for cell sorting and Luminex analysis; the sequencing core for library preparation and sequencing; Yajun Chestnut for technical assistance; Yagai Yang, Joy Wang, and Evangeline Toy for their help with *in vivo* studies.

Note

Supplementary data for this article are available at Cancer Immunology Research Online (http://cancerimmunolres.aacrjournals.org/).

Received December 19, 2023; revised February 15, 2024; accepted March 15, 2024; published first March 15, 2024.

References

1. Sharma P, Allison JP. Immune checkpoint targeting in cancer therapy: toward combination strategies with curative potential. Cell 2015;161:205–14.
2. Mellman I, Chen DS, Powles T, Turley SJ. The cancer-immunity cycle: indication, genotype, and immunotype. Immunity 2023;56:2188–205.
3. Zitvogel L, Galluzzi L, Kepp O, Smyth MJ., Kroemer G. Type I interferons in anticancer immunity. Nat Rev Immunol 2015;15:405–14.
4. Propper DJ, Balkwill FR. Harnessing cytokines and chemokines for cancer therapy. Nat Rev Clin Oncol 2022;19:237–53.
5. Demaria O, Cornen S, Daëron M, Morel Y, Medzhitov R, Vivier E. Harnessing innate immunity in cancer therapy. Nature 2019;574:45–56.
6. Simpson SR, Hemphill WO, Hudson T, Perrino FW. TREX1: apex predator of cytosolic DNA metabolism. DNA Repair (Amst) 2020;94:102894.
7. Mohr L, Toufektchan E, von Morgen P, Chu K, Kapoor A, Maciejowski J. ER-directed TREX1 limits cGAS activation at micronuclei. Mol Cell 2021;81:724–38.e9.
8. Stetson DB, Ko JS, Heidmann T, Medzhitov R. Trex1 prevents cell-intrinsic initiation of autoimmunity. Cell 2008;134:587–98.
9. Schubert N, Schumann T, Daum E, Flade K, Ge Y, Hagedorn L, et al. Genome replication is associated with release of immunogenic DNA waste. Front Immunol 2022;13:880413.
10. Samson N, Ablasser A. The cGAS–STING pathway and cancer. Nat Cancer 2022;1–12.
11. Gao D, Li T, Li X-D, Chen X, Li Q-Z, Wight-Carter M, et al. Activation of cyclic GMP-AMP synthase by self-DNA causes autoimmune diseases. Proc Natl Acad Sci USA 2015;112:E5699–705.
12. Gall A, Treuting P, Elkon KB, Loo Y-M, Gale M, Barber GN, et al. Autoimmunity initiates in nonhematopoietic cells and progresses via lymphocytes in an interferon-dependent autoimmune disease. Immunity 2012;36:120–31.
13. Morita M, Stamp G, Robins P, Dulic A, Rosewell I, Hrivnak G, et al. Gene-targeted mice lacking the Trex1 (DNase III) 3′→5′ DNA exonuclease develop inflammatory myocarditis. Mol Cell Biol 2004;24:6719–27.
14. Gray EE, Treuting PM, Woodward JJ, Stetson DB. Cutting edge: cGAS is required for lethal autoimmune disease in the Trex1-deficient mouse model of aicardi–goutières syndrome. J Immunol 2015;195:1939–43.
15. Crow YJ, Chase DS, Schmidt JL, Szynkiewicz M, Forte GMA, Gornall HL, et al. Characterization of human disease phenotypes associated with mutations in TREX1, RNASEH2A, RNASEH2B, RNASEH2C, SAMHD1, ADAR, and IFIH1. Am J Méd Genet Part A 2015;167:296–312.
16. Günther C, Meurer M, Stein A, Viehweg A, Lee-Kirsch MA. Familial chilblain lupus – a monogenic form of cutaneous lupus erythematosus due to a heterozygous mutation in TREX1. Dermatology 2009;219:162–6.
17. Crow YJ, Hayward BE, Parmar R, Robins P, Leitch A, Ali M, et al. Mutations in the gene encoding the 3′-5′ DNA exonuclease TREX1 cause Aicardi-Goutières syndrome at the AGS1 locus. Nat Genet 2006;38:917–20.
18. Kwon J, Bakhoum SF. The cytosolic DNA-sensing cGAS–STING pathway in cancer. Cancer Discov 2020;10:26–39.
19. Vanpouille-Box C, Alard A, Aryankalayil MJ, Sarfraz Y, Diamond JM, Schneider RJ, et al. DNA exonuclease Trex1 regulates radiotherapy-induced tumour immunogenicity. Nat Commun 2017;8:15618.
20. Gaublomme JT, Li B, McCabe C, Knecht A, Yang Y, Drokhlyansky E, et al. Nuclei multiplexing with barcoded antibodies for single-nucleus genomics. Nat Commun 2019;10:2907.
21. Stuart T, Butler A, Hoffman P, Hafemeister C, Papalexi E, Mauck WM, et al. Comprehensive integration of single-cell data. Cell 2019;177:1888–902.e21.
22. Germain P-L, Lun A, Meixide CG, Macnair W, Robinson MD. Doublet identification in single-cell sequencing data using scDblFinder. F1000Research. 2021;10:979.
23. Andreatta M, Berenstein AJ, Carmona SJ. scGate: marker-based purification of cell types from heterogeneous single-cell RNA-seq datasets. Bioinformatics 2022;38:2642–4.
24. Kotliar D, Veres A, Nagy MA, Tabrizi S, Hodis E, Melton DA, et al. Identifying gene expression programs of cell-type identity and cellular activity with single-cell RNA-Seq. eLife 2019;8:e43803.
25. Wu TD, Reeder J, Lawrence M, Becker G, Brauer MJ. Statistical genomics, methods and protocols. Methods Mol Biol 2016;1418:283–334.
26. Robinson MD, McCarthy DJ, Smyth GK. edgeR: a Bioconductor package for differential expression analysis of digital gene expression data. Bioinformatics 2010;26:139–40.
27. Lun ATL, Chen Y, Smyth GK. Statistical genomics, methods and protocols. Methods Mol Biol 2016;1418:391–416.
28. Wu T, Hu E, Xu S, Chen M, Guo P, Dai Z, et al. clusterProfiler 4.0: A universal enrichment tool for interpreting omics data. Innov 2021;2:100141.
29. Grieves JL, Fye JM, Harvey S, Grayson JM, Hollis T, Perrino FW. Exonuclease TREX1 degrades double-stranded DNA to prevent spontaneous lupus-like inflammatory disease. Proc Natl Acad Sci USA 2015;112:5117–22.
30. Mackenzie KJ, Carroll P, Martin C-A, Murina O, Fluteau A, Simpson DJ, et al. cGAS surveillance of micronuclei links genome instability to innate immunity. Nature 2017;548:461–5.
31. Harding SM, Benci JL, Irianto J, Discher DE, Minn AJ, Greenberg RA. Mitotic progression following DNA damage enables pattern recognition within micronuclei. Nature 2017;548:466–70.
32. Cheng S, Li Z, Gao R, Xing B, Gao Y, Yang Y, et al. A pan-cancer single-cell transcriptional atlas of tumor infiltrating myeloid cells. Cell 2021;184:792–809.
33. Bill R, Wirapati P, Messemaker M, Roh W, Zitti B, Duval F, et al. CXCL9:SPP1 macrophage polarity identifies a network of cellular programs that control human cancers. Science 2023;381:515–24.
34. Fridman WH, Pagès F, Sautès-Fridman C, Galon J. The immune contexture in human tumours: impact on clinical outcome. Nat Rev Cancer 2012;12:298–306.
35. Philip M, Schietinger A. CD8+ T cell differentiation and dysfunction in cancer. Nat Rev Immunol 2022;22:209–23.